Feature-based analysis of a turbulent boundary layer under spanwise wall oscillation

Kempaiah, Kushal U.; Scarano, Fulvio

DOI
10.1063/5.0127220

Publication date
2022

Document Version
Final published version

Published in
Physics of Fluids

Physics of Fluids

Feature-based analysis of a turbulent boundary layer under spanwise wall oscillation

Cite as: Phys. Fluids **34**, 115152 (2022); https://doi.org/10.1063/5.0127220
Submitted: 20 September 2022 • Accepted: 03 November 2022 • Accepted Manuscript Online: 05 November 2022 • Published Online: 29 November 2022

Kushal U. Kempaiah and Fulvio Scarano

Physics of Fluids ARTICLE scitation.org/journal/phf

Feature-based analysis of a turbulent boundary layer under spanwise wall oscillation

Cite as: Phys. Fluids **34**, 115152 (2022); doi: 10.1063/5.0127220
Submitted: 20 September 2022 · Accepted: 3 November 2022 ·
Published Online: 29 November 2022

Kushal U. Kempaiah[a] and Fulvio Scarano

AFFILIATIONS

Faculty of Aerospace Engineering, Delft University of Technology, Delft, The Netherlands

[a]Author to whom correspondence should be addressed: k.ujjainikempaiah@tudelft.nl

ABSTRACT

Spanwise wall oscillations alter the organization of low-speed streaks and ejections in turbulent boundary layers, eventually leading to skin friction drag reduction. Such flow regimes are represented by pointwise statistics or spatial correlation. This work attempts to quantify the systematic distortions of the dominant turbulent structures by feature-analysis, intended to overcome the dispersion observed in pointwise statistics and correlation functions. Furthermore, data from tomographic particle image velocimetry are employed to clarify the mechanism that inhibits hairpin auto-generation, as described in Kempaiah *et al.* ["3-dimensional particle image velocimetry based evaluation of turbulent skin-friction reduction by spanwise wall oscillation," Phys. Fluids **32**(8), 085111 (2020)]. Based on the instantaneous distribution of Reynolds stresses, a specific spatial template is defined for low-speed streaks and flow ejections. Events corresponding to this template are collected and parametrized with their occurrence, geometrical properties (length and orientation), and dynamics (intensity). The approach is compared with most practiced statistical analysis to explain the significance of the features extracted by the detection algorithm in relation to the drag reduction mechanism. Data comparing stationary and oscillating wall in a drag-reducing regime ($A^+_{osc} = 100$, $T^+_{osc} = 100$) are investigated in the near-wall region ($y^+ < 100$). Ejections and low-speed streaks systematically exhibit a positive pitch, supporting the hypothesis that only the rear region, close to the wall, is affected by the wall motion. A side-tilt of elongated ejection events is observed past the phase of maximum oscillation velocity, which is hypothesized to inhibit hairpin auto-generation. The latter indicates a phase dependence of the side-tilt in the oscillating regime. The results also indicate that low-speed streaks and ejection events are reduced by approximately 10% and 15%, respectively, compared with the stationary wall, further consolidating the mechanism of rapid lateral distortion being responsible for the different organizations of the turbulent structures in the near-wall region.

I. INTRODUCTION

One of the primary disadvantages of wall-bounded turbulent flows is the increase in skin-friction drag. Over the last 40 yr, many techniques have been developed to curtail the negative impacts of increased skin friction (Cimarelli *et al.*, 2013, Leschziner, 2020). Among them, spanwise wall oscillation is reported to produce reductions of up to 45% at optimum oscillation amplitude and frequency (Quadrio and Ricco, 2004). In a recent experimental study (Kempaiah *et al.*, 2020), the authors performed direct wall-shear measurements using high-resolution planar particle image velocimetry (PIV). Skin-friction reductions of up to 15% were quantified for a turbulent boundary layer (TBL) at $Re_\theta = 1000$. The quantitative visualization of velocity and vorticity fields by planar and tomographic PIV suggested that the principal mechanism of such reduction lies in the inhibition of hairpin auto-generation near the wall due to the distortion of the low-speed streaks underneath. Furthermore, the availability of streamwise-wall normal velocity distribution from the fully three-dimensional velocity field from tomographic PIV experiments provides the opportunity to quantitatively analyze the effect of wall oscillations on the coherent structures in the flow. Such distortions are frequently observed, but bringing statistical evidence of their modified features is a daunting task due to their random and jittery appearance.

Early observations of structures in a TBL were made from the flow visualization experiments of Kline *et al.* (1967). Streamwise elongated features of high and low velocity were observed in the near-wall regions and termed as streaks. The low-speed streaks were seen to oscillate as they were lifted from the wall leading to a breakup/burst, ascribed to the production of Reynolds shear stresses (RSS) and turbulent kinetic energy (TKE). Quantitative information regarding the near-wall dynamics was obtained by employing techniques such as

quadrant decomposition (Wallace *et al.*, 1972) and variable interval time averaging (Blackwelder and Kapaln, 1976) through the data from hotwire anemometry. The results reported that the events corresponding to the second and fourth quadrant (Q2 and Q4) were termed as ejections ($-u'$ and $+v'$) and sweeps ($+u'$ and $-v'$), primarily contributed to the RSS and TKE production (Lu and Willmarth, 1973). Pointwise measurement techniques do not provide an understanding of the entire spatial organization behind the mechanisms that drive the near-wall dynamics. Flow visualization experiments by Head and Bandopadyay (1981) reported shapes corresponding to hairpin vortices, later confirmed by Wallace (1985). The first direct numerical simulation (DNS) by Moin *et al.* (1986) showed the presence of hairpins through the visualizations of vorticity lines in the vicinity of Q2 events, strengthening the interlink between hairpins and ejection events. The subsequent development of PIV enabled quantitative visualizations of two-dimensional instantaneous flow fields. Adrian *et al.* (2000) reported the existence of vortices that were interpreted as heads of hairpins, which were previously observed to account for the Q2 and Q4 Reynolds shear stresses. The model of hairpin packets was prosed based on the findings from planar-PIV.

Furthermore, tomographic PIV measurements by Jodai and Elsinga (2016) captured the hairpin auto-generation process through time-resolved measurements and reported that hairpin auto-generation time is 30 wall-scaled time units. Ganapathisubramani *et al.* (2003) used planar-PIV data in the wall parallel plane to implement a feature detection algorithm to assess the contribution to the RSS by a packet of hairpins. Recent work by Bae and Lee (2021) analyzed the life cycle of streaks in the buffer layer by tracking streaks in spatially and temporally resolved flow fields by applying feature detection based on a threshold value. The response of streaks and ejections to wall oscillations is not reported in the literature due to the limitations of some of the techniques mentioned above. The combination of conditional sampling and the three-dimensional experimental data enables the application of feature detection techniques tailored to identify and analyze the features to understand the effect of the wall oscillations.

The development of flow control techniques for near-wall turbulence occurred in conjunction with understanding the dynamics of near-wall turbulence. The development of spanwise wall oscillation started from the works of Jung *et al.* (1992). Shear stress reductions were obtained, and an optimum period of oscillations ($T^+_{osc} = 100$) was identified. Experiments were then conducted based on the concept of oscillating walls (OWs) by Laadhari *et al.* (1994), where the reductions obtained from DNS were confirmed. Quadrio and Ricco (2004) performed a parametric study using channel flow DNS at $Re_\tau = 200$ to parametrize drag reduction as a function of oscillation amplitude and frequency. A maximum reduction of skin-friction drag of 45% was reported at $T^+_{osc} = 100$. A subsequent DNS study by Touber and Leschziner (2012) at $Re_\tau = 1000$ ascribed the drag reduction to the rapid distortion of the near-wall streaks, indicating that drag reduction reduces by increasing the Reynolds number. However, Marusic *et al.* (2021) recently postulated that a more effective drag reduction at high Reynolds number conditions could be achieved with wall-oscillation frequencies on the order of large, outer-scaled flow features. The connection between the drag reductions and the coherent structures of the flow has been highlighted in most of the research works described. However, a complete understanding of the physical mechanism and quantification of the response of the flow structures is not achieved yet. Choi (2002) hypothesized that the obtained drag reduction was due to the presence of a spanwise vortex as associated with the change in the shape of the mean velocity profile. Baron and Quadrio (1995) instead pointed attention to the thickness of the Stokes layer. In a more recent study by Yakeno *et al.* (2014), the phase dependence of the quadrant events was undertaken by a conditional sampling of a streamwise vortex of a specific directionality corresponding to different phases of the wall oscillation. A sustained reduction of Q2 events throughout the phase of the wall oscillation was observed, whereas the Q4 sweep events were increased for certain phases of the wall oscillation. Therefore, the connection between the Q2/Q4 events appears to be related to the phase of the wall oscillation. It is, indeed, identified through the literature on drag reductions by spanwise wall oscillation that there is a direct interplay between the two. Yet, a clear quantitative analysis of the distortion of these features is missing.

From the mechanism proposed by the authors (Kempaiah *et al.*, 2020), the rapid distortion of the streaks at their tail significantly inhibits the formation and growth of new "younger" hairpins from a preexisting packet. As a whole, this condition impedes hairpin auto-generation. Such distortion has been hypothesized and qualitatively visualized and illustrated. However, quantifying distorted features like streaks, ejections, and reduction in the number of hairpins occurring in a packet has not been afforded due to the complexity of their three-dimensional organization and jittery occurrence. The present work employs the tomographic PIV data and compares a feature detection algorithm with the more commonly used spatial correlation operators. To this end, tomographic PIV phase-locked data provide the opportunity to examine the details of the distortion mechanism by phase-averaged analysis during the oscillatory motion of the wall.

II. EXPERIMENTAL SETUP

A. Flow facility and boundary layer properties

The experiments were conducted in the open-return low-speed facility W-tunnel at the faculty of aerospace engineering at TU Delft. For more details regarding the experimental setup, data acquisition, and PIV processing parameters, the reader is referred to Kempaiah *et al.* (2020). The turbulent boundary layer properties were calculated from planar-PIV data and are summarized in Table I.

B. Tomographic PIV and assessment of measured velocity

The three-dimensional velocity fields within the TBL were measured by tomographic PIV (Elsinga *et al.*, 2006). The measurement volume for tomographic-PIV is placed 0.25 m (2500 wall units) downstream of the leading edge of the oscillating wall with the dimensions of $70 \times 60 \times 5.7\,mm^3$, corresponding to $700 \times 600 \times 57$ wall units in the streamwise, spanwise, and wall-normal directions [refer to Fig. 1(a)]. The average imaging magnification is $M = 0.2$, with a digital

TABLE I. Turbulent boundary layer properties.

Re_θ	Re_τ	U (m/s)	δ_{99} (mm)	δ^* (mm)	Θ (mm)	u_τ (m/s)	$1y^+$ (mm)	H
980	570	3.0	59.0	6.7	4.9	0.145	0.10	1.36

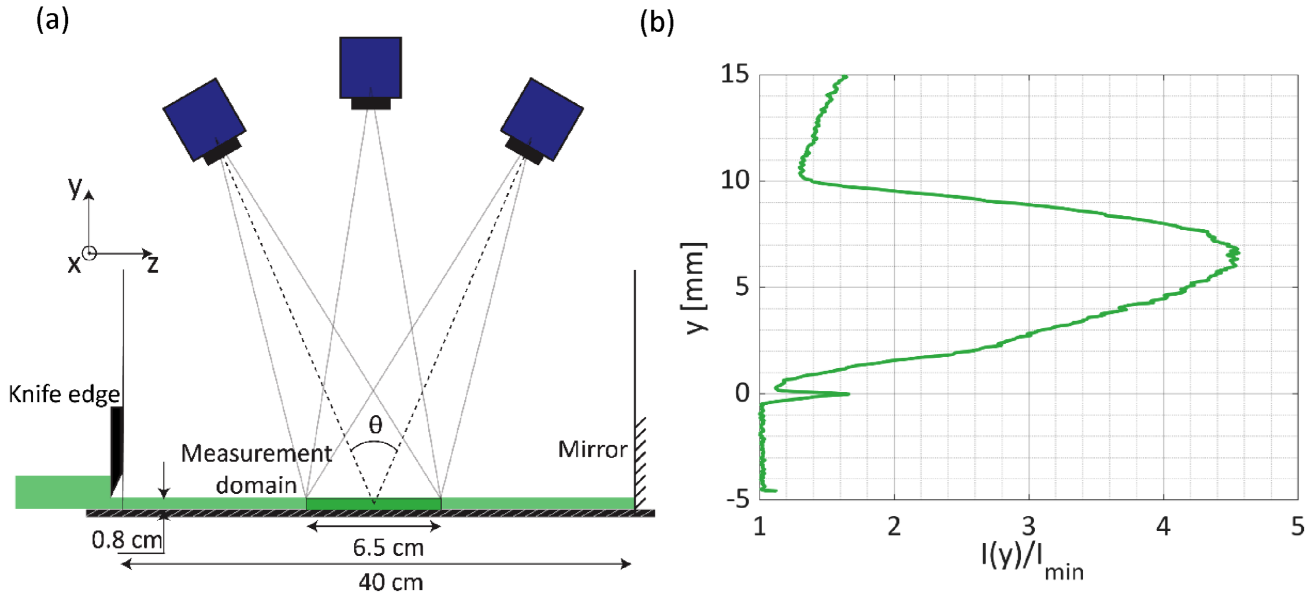

FIG. 1. Illustration of the tomographic setup (a). Average particle light intensity reconstruction I(y), in the wall-normal direction. [Normalized to the minimum intensity (I_{min}) (b).]

resolution of 32 pixels/mm. The instantaneous particle distribution was reconstructed by implementing the MART tomographic algorithm with five iterations (Elsinga *et al.*, 2006). The cross correlation analysis returns $293 \times 246 \times 24$ velocity vectors using an interrogation volume size of 32^3 voxels giving a vector spacing of 0.25 mm (2.5 wall units) with 75% overlap. Phase averaged acquisitions of the tomographic data were obtained at phases with a shift of $\pi/4$ in the sinusoidal oscillations [$Z(\phi) = A_{osc}\sin(\phi)$] of the wall at the phase interval of $\pi/4$. The conditions $\phi = 0$ and $\phi = \pi$ are labeled as "high-speed," $\phi = \pi/4$ and $\phi = 5\pi/4$ as "decelerating," $\phi = \pi/2$ and $\phi = 3\pi/2$ as "low-speed," and $\phi = 3\pi/4$ and $\phi = 7\pi/4$ as "accelerating." Differently from the tomographic-PIV experiment, in the data from the planar-PIV, the phase of oscillation is not monitored.

The position of the wall within the measurement volume was determined by plotting the average particle light intensity reconstruction [I(y)] normalized to the minimum intensity (I_{min}) in the domain [Fig. 1(b)]. The error in the position of the wall was found to be 300 μm corresponding to three wall units and has been corrected, leaving an uncertainty of 50 μm. The mean velocity profile returned by tomographic PIV compares well with both the planar PIV measurements and the DNS data at $Re_\theta = 1000$ by Schlatter and Örlü (2010) [Fig. 2(a)]. For the tomographic measurements, the inspected volume

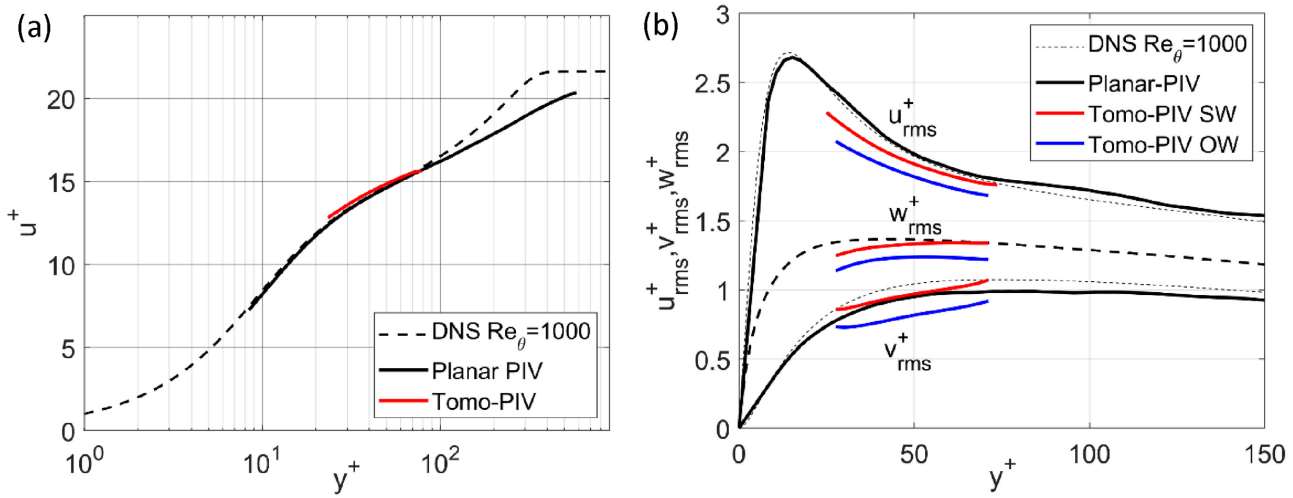

FIG. 2. Mean (a) and root mean square (r.m.s.) (b) velocity profiles returned by tomographic PIV using cubic and elongated correlation volumes were compared against the DNS database of Schlatter and Örlü (2010), and the planar-PIV data from Kempaiah *et al.* (2020) scaled with u_τ of the stationary wall (SW).

spanned a limited wall-normal range ($20 < y^+ < 70$) due to the light intensity decreasing close to the wall, leading to a more frequent occurrence of ghost particles. Therefore, the measurement volume is limited in the above range. The root mean square (r.m.s) fluctuations of the velocity components are presented and compared against the same DNS database in Fig. 2(b). It is clear from the streamwise velocity component that the near-wall peak at $y^+ = 15$ has not been captured. The u^+_{rms} profiles show lower values with respect to the DNS, but the difference remains within 6%, similar to other studies employing the same technique (Jodai and Elsinga, 2016). Based on the observations, the data are considered suited for the analysis of instantaneous flow features in the range of $20 < y^+ < 70$.

C. Data reduction

1. Two-point correlation

The statistical analysis of velocity fluctuations in turbulent boundary layers is most frequently performed by spatial two-point correlation (Tong *et al.*, 2022). Early adoption of the technique for three-dimensional tomographic datasets is reported by Schröder *et al.* (2011). The two-point correlation R between two quantities A and B is defined as

$$R_{AB} = \frac{\overline{A(x,y)B(x+\Delta x, y+\Delta y)}}{\sigma_A \sigma_B}, \tag{1}$$

where the product $\sigma_A\sigma_B$ normalizes the upper inner product by the standard deviation of the quantities. Given that the process of turbulent kinetic energy production is linked to the ejections ($u'v'$) and to the low-speed streaks (u'), the velocity fluctuations in the streamwise (u') and wall-normal (v') direction will be analyzed.

2. Feature detection algorithm

As opposed to two-point correlations, feature detection is based on a segmentation of the spatial domain. Most commonly, the segmentation criterion requires defining a threshold value for the property of interest. Here, we refer to the level of velocity fluctuations [refer to Fig. 4(a)] as obtained from tomographic-PIV. Streaks and ejections are the features of interest, and they are expected to be approximately aligned in the streamwise direction for the stationary wall. The sidewise motion propagating through the stokes layer, instead, causes the lower portions of these features to move sideways, causing their side-tilt. It is expected, based on the hairpin-packets paradigm (Adrian *et al.*, 2000, Adrian, 2007, Jodai and Elsinga, 2016), that the aft part of such ejection regions is also at a lower distance from the wall.

Detection functions are defined in Table II for the streamwise velocity fluctuations ($F_d^{u'}$, low-speed streaks) and the product of streamwise wall-normal fluctuations ($F_d^{u'v'}$, ejections). Such functions are normalized to the local fluctuation by the global root mean square value (u_{rms}, v_{rms}, w_{rms}) of the stationary wall. The detection algorithm adopted here is similar to that reported by Martins *et al.* (2019). It is described in the following steps, and it is illustrated in Fig. 4 (multimedia view).

The quantities of interest for these features are their size (length), spatial occurrence, and inclination. For the latter, the rotation with respect to the streamwise axis in the x–y plane is termed α (pitch), and in the x–z plane is termed γ (tilt). The above is schematically illustrated in Fig. 3, where a detected feature is pictured while affected by the wall motion. A reference value for the tilt angle γ_0 can be inferred from the ratio of amplitude oscillation and the length of the distorted structure,

$$\gamma_0 = \tan^{-1}\left(\frac{A}{L}\right). \tag{2}$$

For the present conditions, $\gamma_0 = 25°$, where the amplitude (A) is 100 wall units, and the average length (L) of a typical structure is 200 wall units (refer to Table III). However, the latter may overestimate the actual tilt, which is reduced under the effect of streamwise convection during the side oscillation.

The detection algorithm is summarized in the following three steps:

(1) Definition of the fluid dynamic property
The velocity fluctuations in the 3D domain [u', v', Fig. 4(a)] are chosen as a basis to define a detection function ($F_d^{u'}$: streaks, $F_d^{u'v'}$: ejections) as the ratio of the local velocity fluctuation with the r.m.s fluctuations [$u'_{rms}(y)$, $u'v'_{rms}(y)$] at the corresponding height for the stationary wall. Figures 4(b) and 4(c) show such detection functions for the streamwise and streamwise-wall-normal fluctuations.

(2) Detection criteria (thresholding)
A threshold value (F_t) for the detection function is used that identifies the boundary of the segmented region for the low-speed streaks ($F_d^{u'} < -1$) and ejections ($F_d^{u'v'} < -1$ and $F_d^{u'} < 0$)

TABLE II. Summary of the feature detection algorithm.

Coherent structure	Detection function	Condition	Threshold (F_t)
Low-speed streaks	$F_d^{u'} = \frac{u'(x,y,z)}{u'_{rms}(y)}$	$F_d^{u'} < F_t^{u'}$	-1
Ejections	$F_d^{u'v'} = \frac{u'v'(x,y,z)}{u'v'_{rms}(y)}$	$F_d^{u'v'} < F_t^{u'v'}$ and $F_d^{u'} < 0$	

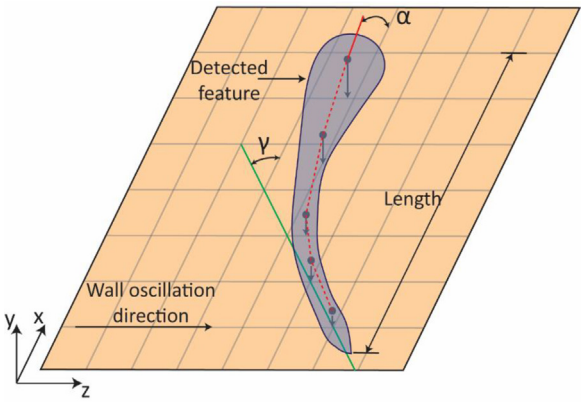

FIG. 3. Schematic illustration of a turbulent structure undergoing distortion due to wall oscillation. Vertical arrows indicate the wall-normal distance. For the given condition, the tail is expected to be shifted sidewise producing an overall tilt (γ).

TABLE III. Length and number of events for streaks and ejections from 3D feature detection.

Case		Streaks ($F_d^{u'} < -1$)		Ejections ($F_d^{u'v'} < -1$ and $F_d^{u'} < 0$)	
		Length (wall units$^+$)	Number of events (per field)	Length (wall units$^+$)	Number of events (per field)
OW	SW	279 ± 7	7.3	194 ± 4	11.2
	$\phi = 0, \pi$	273 ± 12	7.0	179 ± 6	10.3
	$\phi = \pi/4, 5\pi/4$	255 ± 8	6.9	174 ± 4	10.3
	$\phi = \pi/2, 3\pi/2$	258 ± 11	7.4	165 ± 6	11.0
	$\phi = 3\pi/4, 7\pi/4$	258 ± 10	7.2	171 ± 6	10.8

events. Based on each criterion, the segmented domain is labeled by a logical (0,1) operator. The sensitivity of the threshold is discussed in the Appendix.

(3) Ensemble of selected structures
Regions that simultaneously satisfy the above two conditions are considered relevant to the analysis as they correspond to the physical mechanisms of interest, i.e., where the flow exhibits significantly retarded flow and considerable ejection activity. Figure 4(d) represents the detected ejection, sectioned at a given wall parallel plane. Table II summarizes the algorithm and its parameters.

The ejection events detected in Fig. 4(d) correspond to the flow regions where low-speed fluid is lifted away from the wall. To obtain quantitative information (length and spatial occupation) from these features in the wall parallel plane, the concept of connected

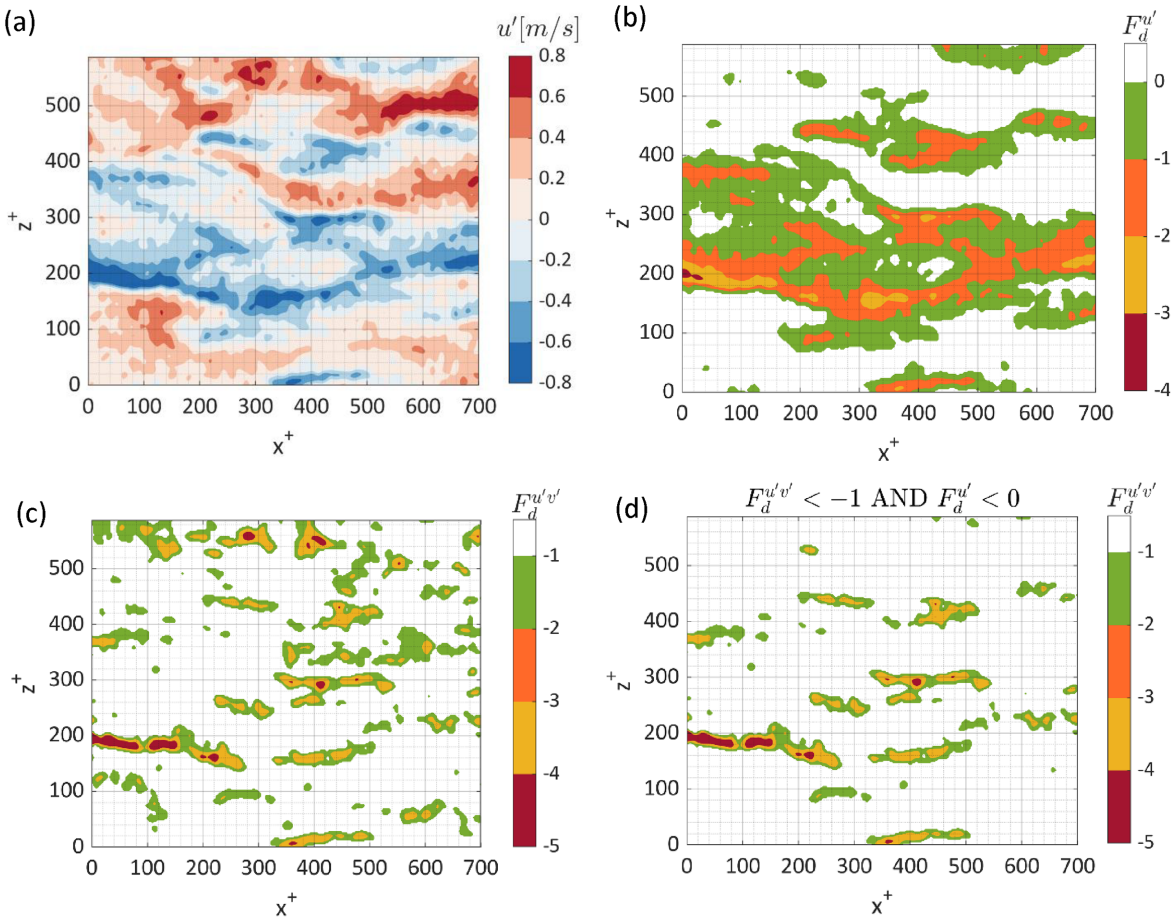

FIG. 4. Illustration of the feature detection algorithm used for identification of streaks and ejection events from the u' velocity field (a), detection of the streaks (b), detection of the ejection and sweep events (c), and, finally, the identified ejection events based on the described detection function (d). The data are from the case of the stationary wall (SW) and correspond to the wall parallel plane at $y^+ = 20$. Multimedia view: https://doi.org/10.1063/5.0127220.1.

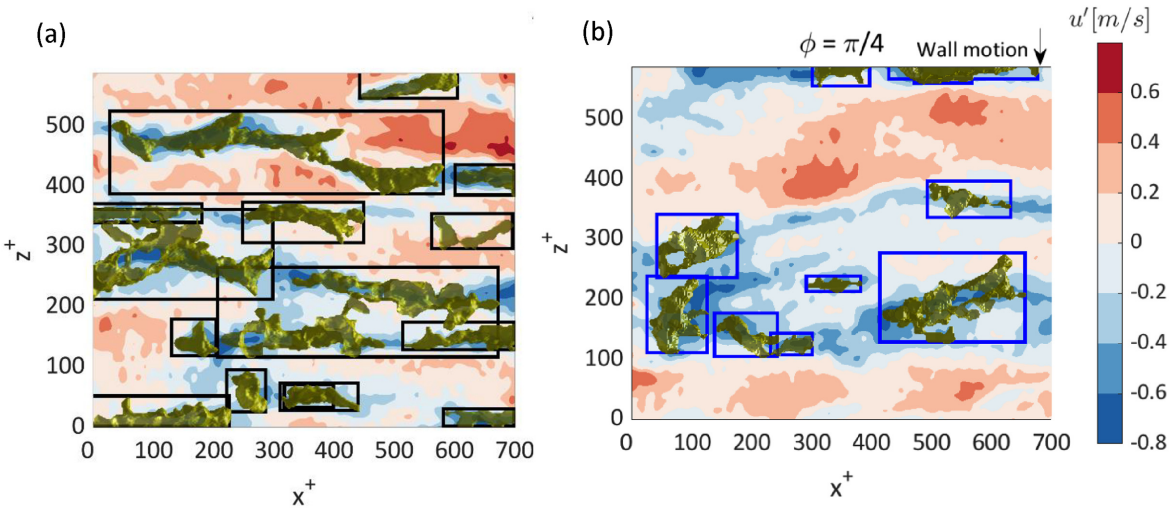

FIG. 5. Iso-surface of ejection events detected through the 3D feature detection algorithm enclosed in boxes for the case of the stationary wall (a) and oscillating wall (OW). The isolated features enclosed in boxes are analyzed further. Multimedia view: https://doi.org/10.1063/5.0127220.2.

components is employed as outlined by Haralick and Shapiro (1992). The method is implemented through the *Matlab* function (*bwlabel*), which analyzes a 2D binary field (i.e., within a specific plane). By such analysis, data points pertaining to the detected streaks and ejections [Fig. 4(d)] are labeled as *ones*. Such points are clustered based on eight-neighbors connectivity [i.e., North (N), South (S), East (E), West (W), NE, NW, SE, and SW]. After this operation, each detected feature is accepted, and the specific information can be extracted. Intrinsic properties are the length and the angle, whereas global properties are their occurrence and spatial occupation. Both are reported and discussed in Sec. III.

The treatment of the features identified, however, is challenged by their highly three-dimensional features. Moreover, quantities of interest like length and inclination (as described in Fig. 4) require the detection of the structures in the whole domain (i.e., in three dimensions). The 3D binary matrix consisting of features represented by ones is clustered by using the function *region3props*, which implements the same procedure described by Haralick and Shapiro (1992) but for a 3D volumetric image regions by creating a 3D bounding box around the detected regions as shown in Figs. 5(a) (SW) and 5(b) (OW corresponding to $\phi = \pi/4$ refer to multimedia view for a comparison using multiple three-dimensional velocity fields) for the stationary and oscillating wall conditions.

The length and inclination of these features are obtained by singular value decomposition (SVD) of the detected regions. The resulting eigenvector yields the orientation of the principal axis (red in Fig. 6), which minimizes the orthogonal square distance. An example is shown in Fig. 6 for a chosen feature. It should be retained in mind, however, that the maximum values of vertical inclination (α) that can be detected are limited by the measurement domain wall normal range of 50 wall units. The individual features reported in Fig. 6 show a smaller sidewise tilt angle of 2.8° for stationary wall, whereas the tilt increases to −13.6°

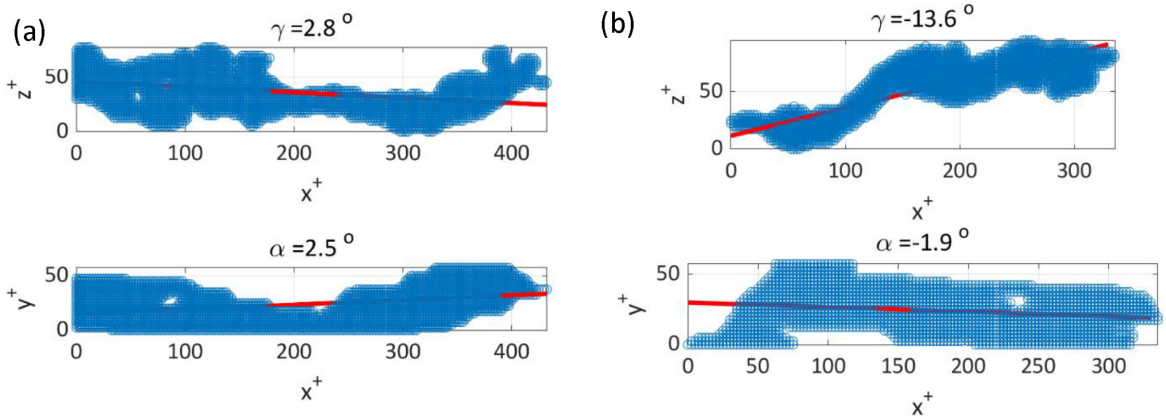

FIG. 6. Detected features corresponding to an ejection event for the case of the stationary wall (a) and oscillating wall for $\phi = \pi/4$ (b) with the SVD eigenvector (in red), which is used to extract the vertical inclination or pitch (α) and spanwise tilt (γ). Multimedia view: https://doi.org/10.1063/5.0127220.3.

when the wall oscillates [during downward motion, arrow in Fig. 5(b)]. The motion of the wall results in a rapid lateral distortion of the ejection events. Close to 500 structures were identified for each phase of the OW and 2000 for the SW. A collection of identified ejection structures is shown in Fig. 6 (multimedia view).

III. RESULTS

A. Analysis by spatial correlation

The two-point statistical correlation of the streamwise velocity fluctuations (u′) is a common tool to inquire about streamwise velocity coherence. This operator returns the pattern of the coherent fluctuations and gives an indication of the flow arrangement into low- and high-speed streaks. The mean result of the correlation analysis is shown here in a wall-parallel (x–z, $y^+ = 20$) and streamwise wall-normal plane (x–y). For the stationary wall, the normalized two-point correlation map of $R_{u'u'}$ [referred to as R_{St1}, Eq. (1)] at a height $y^+ = 20$ and wall-normal planes $R_{u'(y^+=20)u'(y^+)}$ (referred to as R_{St2}) are shown in Fig. 7. The correlation map for the stationary wall [SW, Fig. 7(a)] exhibits an elongated structure with two side-lobes along the span. The central structure is consistent with the streaky pattern of low-high velocity fluctuations. However, the side lobes are underestimated in length as a result of their jittery occurrence. The result for the oscillating wall (OW, ensemble average irrespective of oscillation phase) is shown in Fig. 7(b). The differences to the SW case are rather minor: for $R_{St1} = 0.05$. The width of the correlation map is 100 wall units for SW compared to 140 for OW, indicating a mild spanwise widening of the positive correlation region when the wall is oscillated. Furthermore, the corresponding length increases from 700 to 900 wall units for OW. Both observations may suggest that the wall oscillation has little to no effect on the length and spacing of the streaks, which is, however, in contrast with the instantaneous observations in Fig. 5, where the streamwise coherence of ejection events is visibly reduced in the oscillating regime. It should be retained in mind that the correlation maps do not provide information about the intensity of these events, but inference can be made from Fig. 2(b) where the OW is reported to have weakened fluctuations. The streamwise fluctuations at $y^+ = 20$ also correlate with the fluctuations at higher wall-normal planes (R_{St2}), as shown in Figs. 7(c) and 7(d). The correlation map indicates a region inclined with the streamwise direction in agreement with the observations of Sillero *et al.* (2014) corresponding to the lift up of the low-speed fluid in the head region.

The periodic nature of the wall oscillations permits the comparison of results in the x–z plane for the corresponding phases of the wall oscillations. The phase dependence of the positive correlation regions corresponding to the different phases [refer to Figs. 8(a)–8(f)] reveals minor differences. In particular, the side-angle γ lies between $-1.5°$ and $1.5°$, suggesting that the low-speed streaks remain essentially aligned streamwise. Such a result is again in contrast with the instantaneous visualizations and may be ascribed to the statistical effect of ensemble averaging.

The analysis is extended to the product of the streamwise wall-normal velocity fluctuations $R_{(u'v')(u'v')}$ (referred to as R_{Ej1}) and in the wall-normal planes $R_{u'v'(y^+=20)u'v'(y^+)}$ (referred to as R_{Ej2}) that signify ejections events. The analysis in the streamwise spanwise plane is made by reporting the autocorrelation maps of R_{Ej1} at $y^+ = 20$ in Figs. 9(a) (SW) and 9(b) (OW). The correlation maps report a similar difference as seen for the streamwise velocity fluctuations, i.e., increase in width (Δz^+) and decrease in length (Δx^+) for the OW corresponding to $R_{Ej1} = 0.05$. The product of the streamwise wall-normal velocity correlations in the wall-normal plane follows the same procedure as that adopted for the streamwise velocity fluctuations. Figures 9(c) (SW) and 9(d) (OW) report R_{Ej2}, indicating that SW ejections tend to be pitched up ($\alpha > 0$), whereas for OW, a more symmetric shape suggests no pitch ($\alpha \sim 0$). The inclination is a characteristic feature of near-wall turbulence, which arises due to the lift-up of low-speed fluid

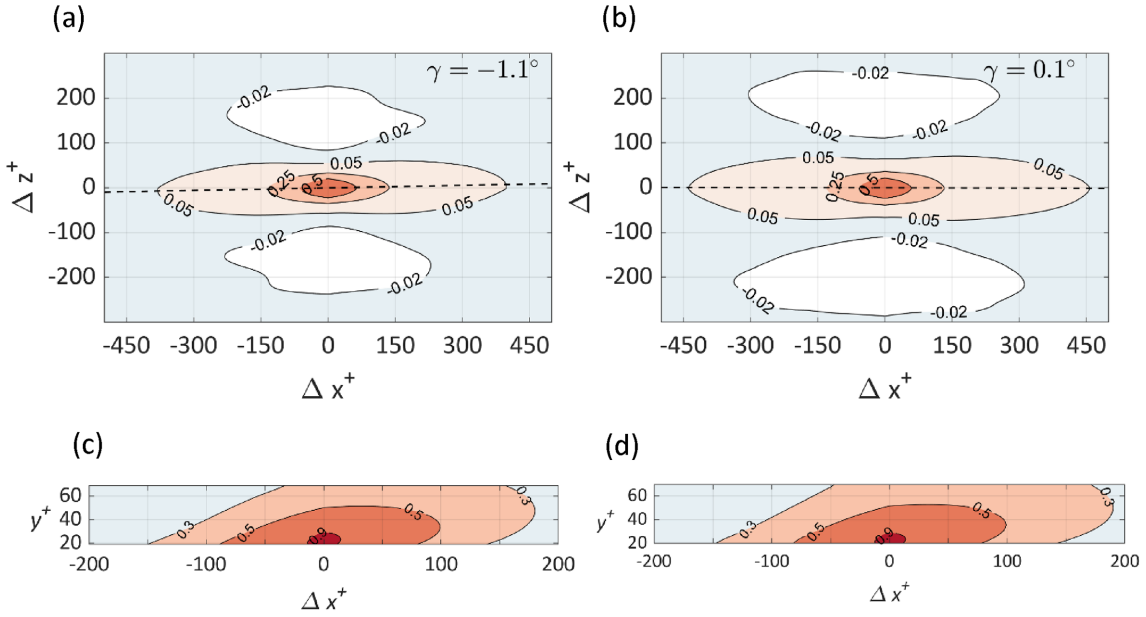

FIG. 7. Two-point autocorrelation of streamwise velocity fluctuations (R_{St1} and R_{St2}) for stationary [SW, (a) and (c)] and oscillating [OW, (b) and (d)] wall at $y^+ = 20$.

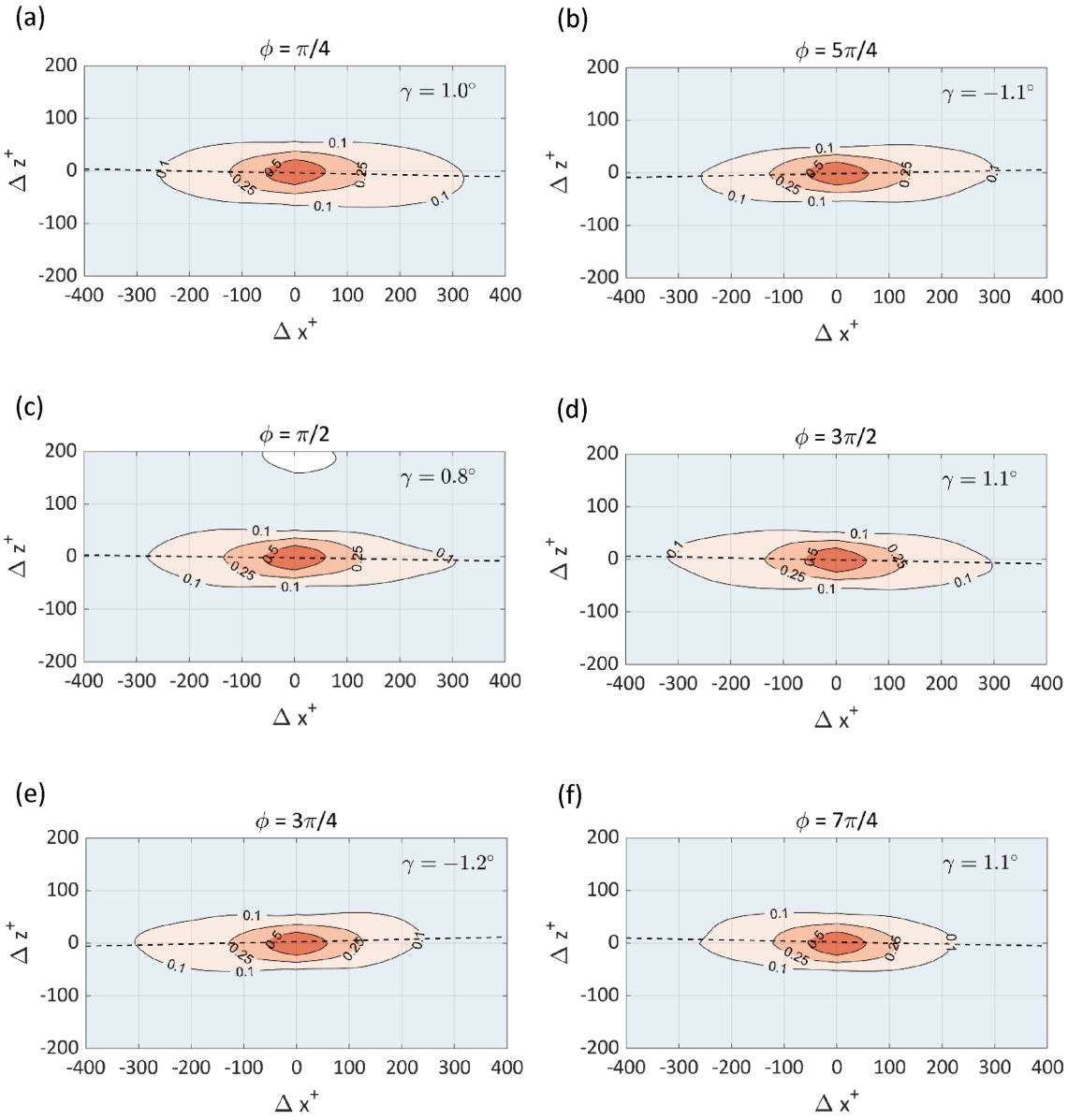

FIG. 8. Comparison of the autocorrelation maps of the streamwise velocity fluctuations (R_{St1}) for the different phases of the oscillating wall. (a) $\phi = \pi/4$, (b) $\phi = 5\pi/4$, (c) $\phi = \pi/2$, (d) $\phi = 3\pi/2$, (e) $\phi = 3\pi/4$, and (f) $\phi = 7\pi/4$.

into higher layers. The phase averaged results in the x–z plane reveal some effects of the wall oscillations (Fig. 10). The sidewise tilt (γ) follows the motion of the wall, as shown already in Fig. 9, but the amplitude of the sidewise tilt is threefold higher (i.e., γ is close to 1° for streaks and 3° for ejections). At $\phi = \pi/4$ and $\pi/2$, the wall is displaced along z and reports a negative γ (−3.5° and −3°). Followed by motion inversion for $\phi = 3\ \pi/4$, where γ is 1.1° [Fig. 10(e)]. The side tilt is lowest at $\phi = \pi/4$, $\pi/2$ due to the re-orienting effect during motion inversion. The phase dependence of the autocorrelation maps of u′v′ at $y^+ = 20$ indicates that wall oscillations do affect ejections in a more pronounced way than the streaks.

In conclusion, the analysis by two-point correlation yields some consistent trends of the distortions induced by wall oscillations. However, given the random occurrence of the turbulent structures and the diffusive nature of the correlation operator, this tool is seen as inadequate to yield detailed information on the distortion of turbulence in the presence of wall oscillation.

B. Analysis by feature detection

The feature detection algorithm aims to increase the observability of distortion events and infer the phase-dependent behavior. In particular, it is expected that the structure's occurrence, length, intensity,

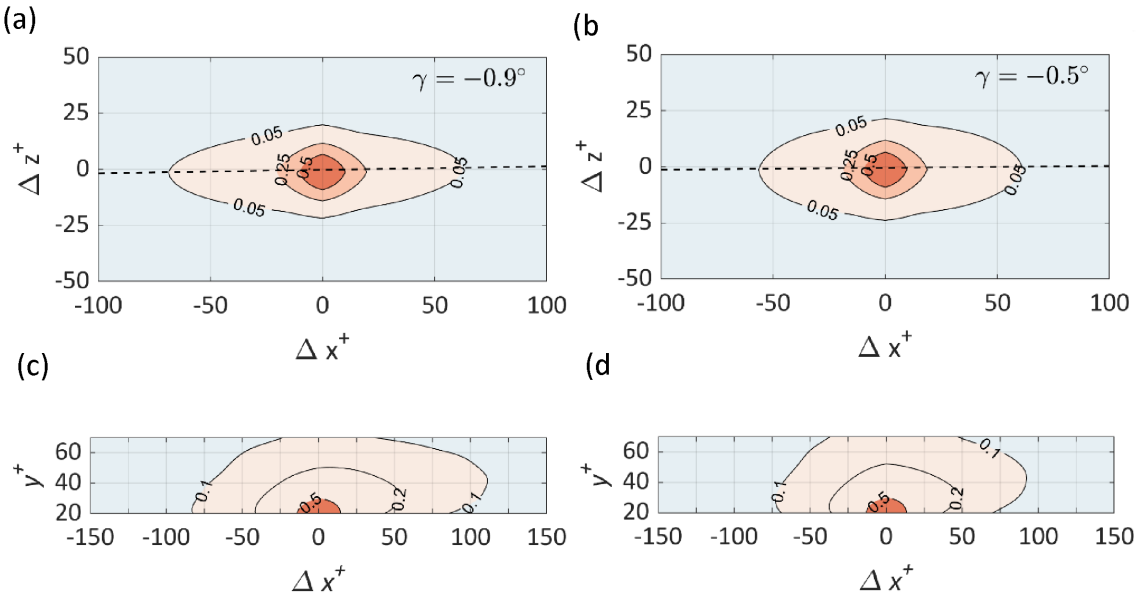

FIG. 9. Autocorrelation map of streamwise-wall normal velocity fluctuations (R_{Ej1}) for stationary [SW, (a)] and oscillating [OW, (b)] wall at $y^+ = 20$; correlation map of streamwise velocity fluctuations at $y^+ = 20$ with different wall-normal heights {R_{Ej2} for stationary [SW, (c)] and oscillating [OW, (d)] wall in the wall normal x–y plane}.

and orientation be deducted more clearly from the instantaneous measurements. A more significant statistical structure is expected to emerge when performing ensemble operations after detection and classification. The tilt angle γ is expected to be correlated with the direction of the wall oscillations, with positive and negative values corresponding to the phase of the wall oscillation. The phase-averaged occurrence of γ for the detected structures (based on streamwise velocity fluctuations) is reported in Fig. 11 and compared to the stationary wall condition. The latter exhibits a symmetrical distribution around $\gamma = 0$. The conditions for the oscillating wall are examined at six values of the phase: $\phi = \{\pi/4, \pi/2, 3\pi/4, 5\pi/4, 3\pi/2, 7\pi/4\}$. Structures exhibit excess in tilt angle consistent with the oscillation direction at typical values significantly large than that observed with the correlation analysis. Yet, a tilt of 10°–20° is consistent with the instantaneous visualizations. Peaks in the histograms are also observed consistently during the two opposite phases of the oscillation cycle, with positive and negative values of γ accordingly. The overall effect is that the histograms representing the occurrence of structure tilt become asymmetric and feature a *hump* corresponding to the sidewise wall motion. When the same analysis is performed considering the joint condition of low-speed and ejection, the data scatter increases, and the correlation of tilt occurrence with the phase of oscillation becomes less evident (Fig. 12). This may also be interpreted as ejections mostly corresponding to the head regions, which have already lifted up in the range $y^+ > 50$, and as such, they are less affected by the wall oscillatory motion. The latter should, however, not lead to the conclusion of ejection motions not being altered by wall oscillation. In fact, they are overall significantly reduced in number and intensity as a result of the shorter extent of such regions caused by the smaller number of hairpins being auto-generated.

Figure 13(a) shows the distribution of the pitch angle α for the detected ejection events. The differences between stationary and oscillating wall here are marginal, which is ascribed to the limited wall-normal extent of the tomographic domain. The distribution of γ, instead, yields a significantly wider spread for OW, indicating a higher probability for larger tilt states compared to the stationary wall. Considering the spanwise motion of the wall with an amplitude of 1 cm and frequency of 15 Hz, the maximum spanwise wall velocity can be approximated to 1 m/s. The mean streamwise velocity in the tomographic domain is close to 2 m/s. The corresponding inclination, that is, expected to be in the region is close to 25°, which can be observed in the increased probabilities of γ in Fig. 13(b). The latter estimate based on kinematic properties falls near the previous estimate of γ_0 based on oscillation amplitude and streak length. It can be concluded that the wall oscillations act by tilting the turbulent structures that contribute to the large Reynolds stresses in the near-wall region. The latter results in the suppression of the near-wall cycle of hairpin auto-generation, ultimately leading to reductions in the local skin-friction drag.

C. Properties, phase statistics, and conceptual model

With the above data, the statistical occurrence and properties of streaks and ejections will be presented, with a comparison between the oscillating and stationary wall. Furthermore, the phase-dependent behavior is accounted for. The section closes with a visual description of a conceptual model that expands on that previously presented by the authors (Kempaiah *et al.*, 2020), including some hypotheses on phase dependence.

Figure 14 depicts the spatial occupation and streamwise length of the streaks identified by feature detection. The analysis is conducted at several heights to infer their occurrence across the boundary layer (x–z plane, refer to Fig. 4). The analysis of spatial occupation of the streaks identified from the detection function ($F_d^{u'} < -1$) yields a presence of

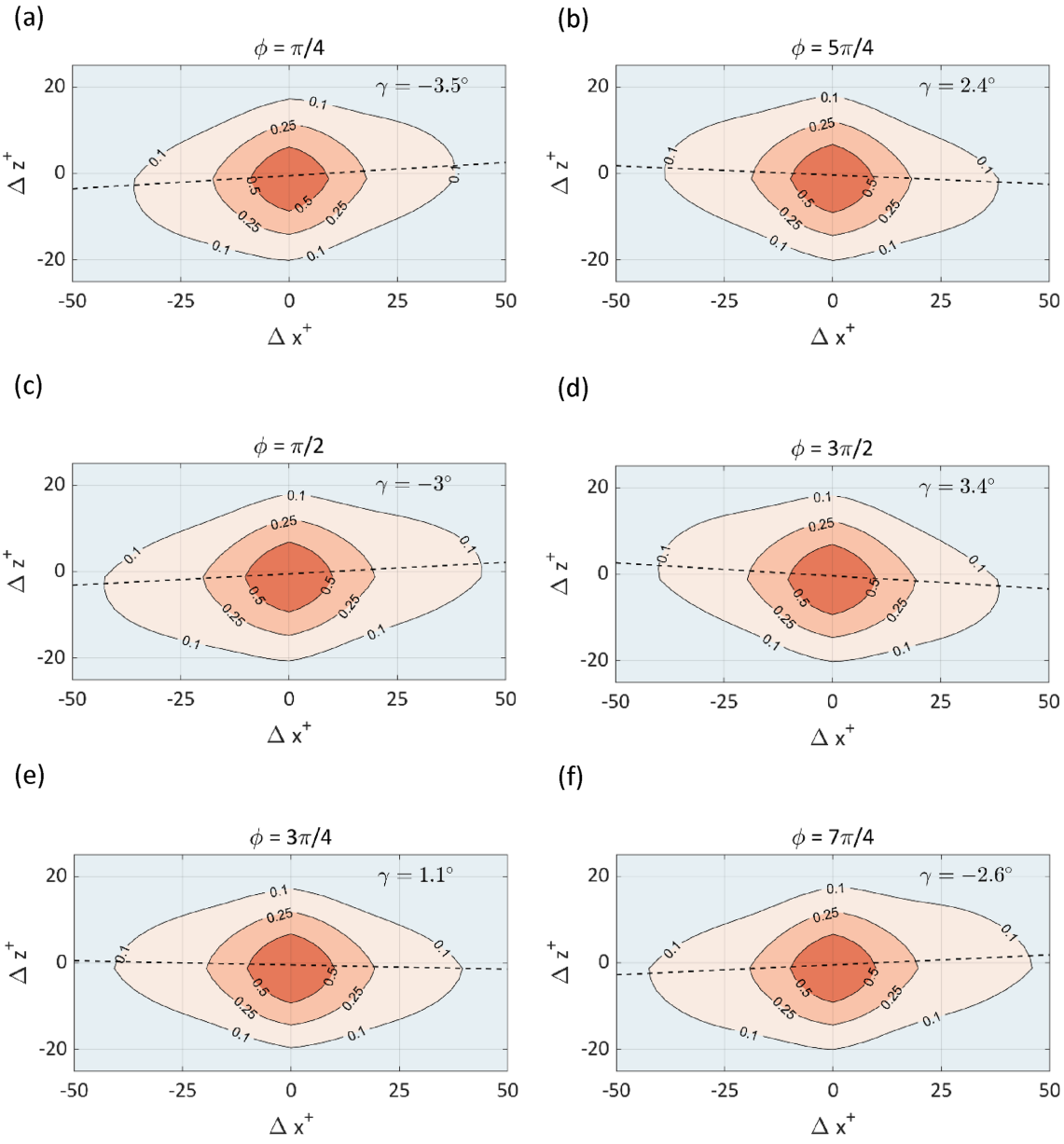

FIG. 10. Comparison of autocorrelation maps of the streamwise-wall normal velocity fluctuations (R_{Ej1}) during the different phases of the oscillating wall. (a) $\phi = \pi/4$, (b) $\phi = 5\pi/4$, (c) $\phi = \pi/2$, (d) $\phi = 3\pi/2$, (e) $\phi = 3\pi/4$, and (f) $\phi = 7\pi/4$.

17% for the stationary wall at a height up to $y^+ = 35$. The same structures have a significantly lower occurrence, peaking at $y^+ = 30$ with 16% and generally remaining below the stationary wall case of approximately 10%. In this analysis, the results of the OW have been phase averaged as the phase dependence is small and not discernible through the feature detection algorithm. The length of the streaks is 10%–20% shorter for the oscillated wall in the near wall region with a crossover at $y^+ = 40$, after which an inversion in length occurs, i.e., the streaks increase in length for the oscillated wall to an extent of 10%. This increase in length of the streaks above 40 wall units suggests that far from the wall, the streaky structure becomes more stable. This is ascribed to the reduced activity of ejection events. The latter hypothesis is consistent with the intensity of the u′ fluctuations being lower in the case of the oscillating wall, as reported earlier [refer to Fig. 2(b)].

The ejection events reported in Fig. 15 show a more marked difference between the stationary and oscillating wall. This supports the observation that the wall oscillations significantly weaken

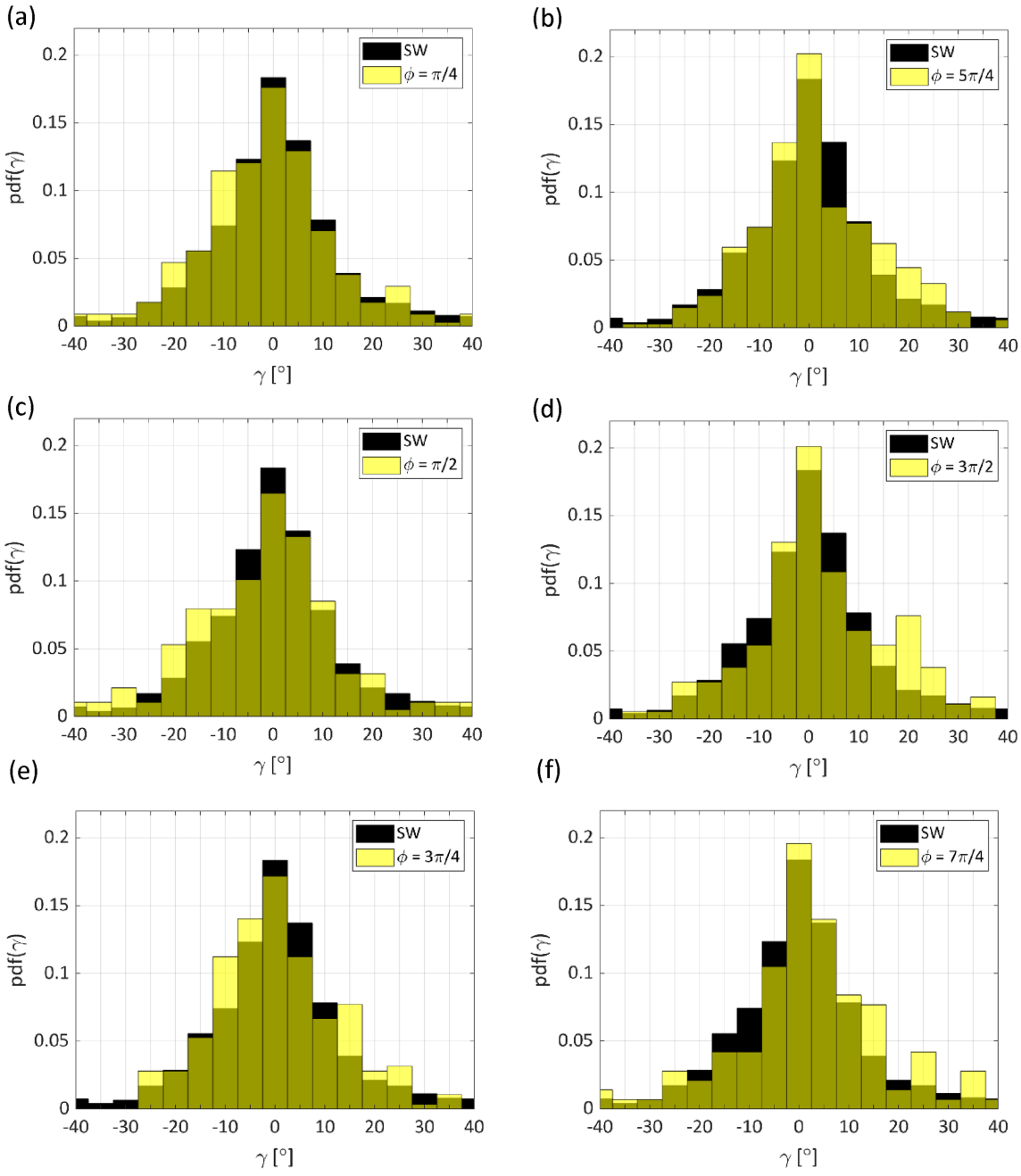

FIG. 11. Probability distribution of sidewise tilt (γ) from detected streaks ($F_d^{u'} < -1$) at six phases of wall oscillation. (a) $\phi = \pi/4$, (b) $\phi = 5\pi/4$, (c) $\phi = \pi/2$, (d) $\phi = 3\pi/2$, (e) $\phi = 3\pi/4$, and (f) $\phi = 7\pi/4$.

vertical velocity fluctuations, in turn attenuating sweeps and skin-friction. The spatial occupation of ejections is reduced from 20% to 40% over the examined domain. The streamwise length of these events exhibits a behavior similar to that of the streaks, with a 10% to 20% shorter length up to 45 wall units. Above this height, an inversion is taking place, but the difference is not discernible. The ejection events in the region above 45 wall units have the same length scales, but the spatial occupation is reduced along with the intensity of these events, which can be observed in Fig. 15(b). For completeness, the phase dependence of these structures, i.e., the low-speed streaks and ejections, is examined, and results are reported in Table III.

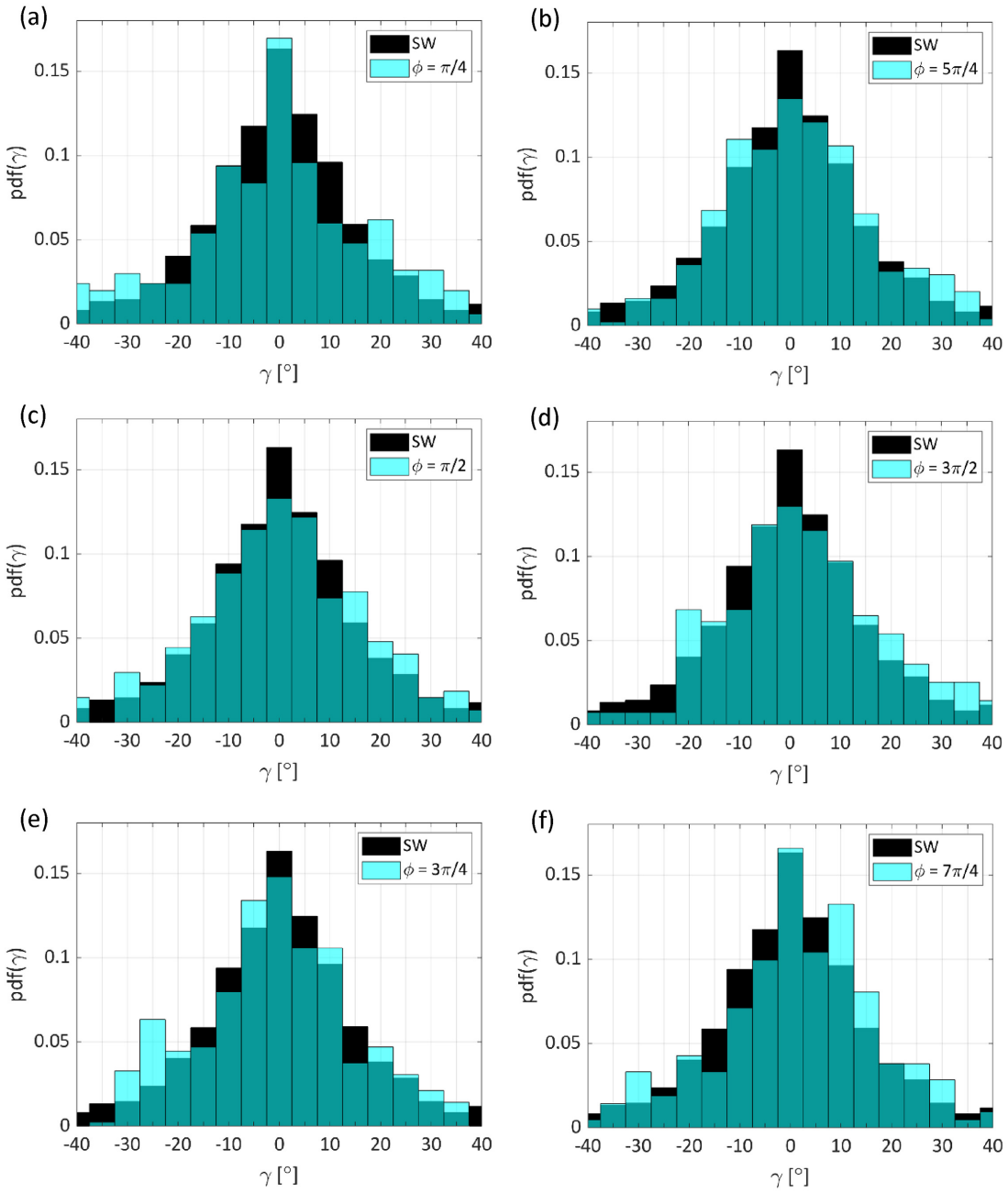

FIG. 12. Probability distribution of sidewise tilt (γ) from detected ejections ($F_d^{u'v'} < -1$ and $F_d^{u'} < 0$) at six phases of wall oscillation. (a) $\phi = \pi/4$, (b) $\phi = 5\pi/4$, (c) $\phi = \pi/2$, (d) $\phi = 3\pi/2$, (e) $\phi = 3\pi/4$, and (f) $\phi = 7\pi/4$.

The results of the 3D algorithm (Table III) show that the length of the streaks is the least when the position of the wall corresponds to $\phi = \pi/4$, $5\pi/4$ with reductions in length of 10%, whereas the average number of detected events remains the same. The length of the streaks moves close to that of the stationary wall when $\phi = 0, \pi$. The same trend is observed for the ejection events, with reductions in the length by 15% in the $\phi = \pi/2, 3\pi/2$. The phase dependence in the coherent structures analyzed is observable, although with a delay due to the wall-normal location of the measurement volume. The process of turbulent kinetic energy production is linked directly to the ejections ($u'v'$) and indirectly to the low-speed streaks (u'). The low-speed streaks are known to oscillate and breakup, leading to

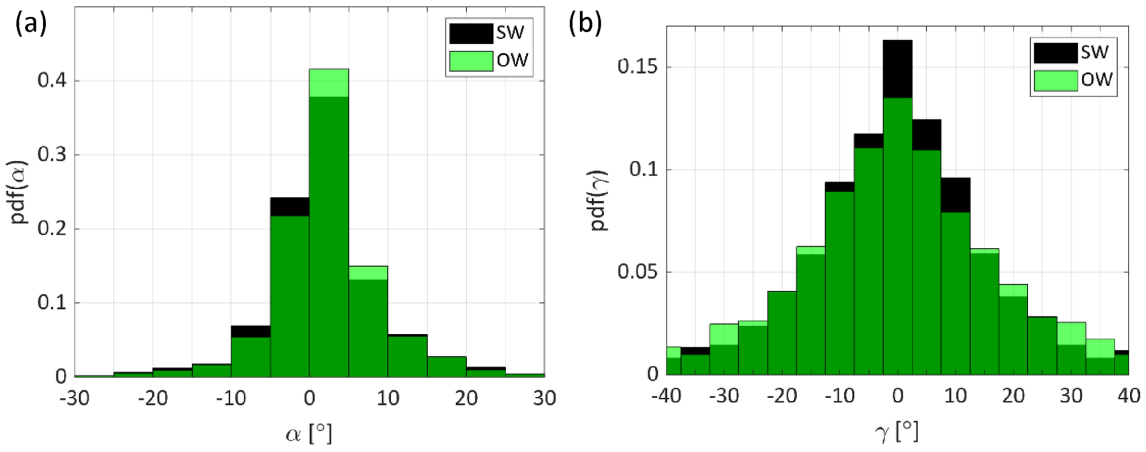

FIG. 13. Comparison of the probability distribution function of α (a) and γ (b) for the stationary and oscillating wall cases of the detected ejection features.

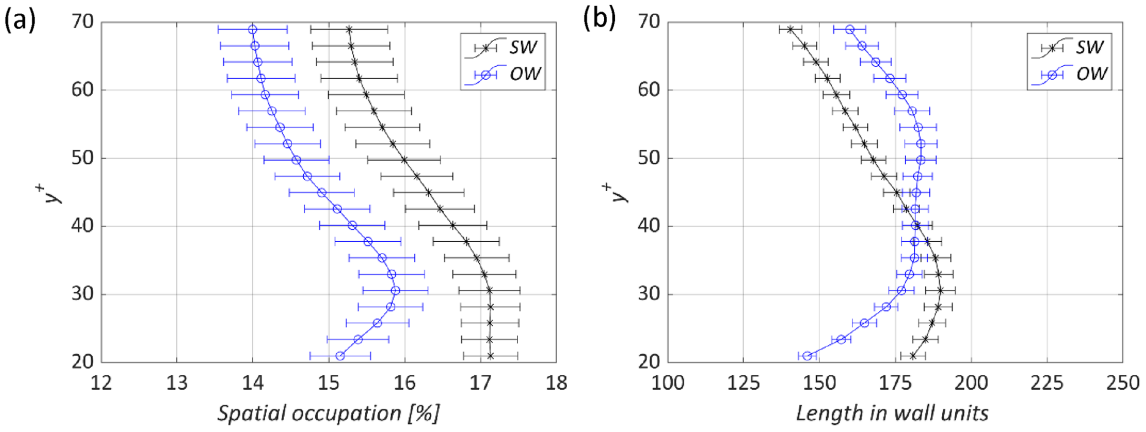

FIG. 14. Distribution of spatial occupation (a) and streamwise length (b) of the detected streaks in the measurement domain from the implementation of feature detection algorithm in each x–z plane corresponding to the wall-normal location.

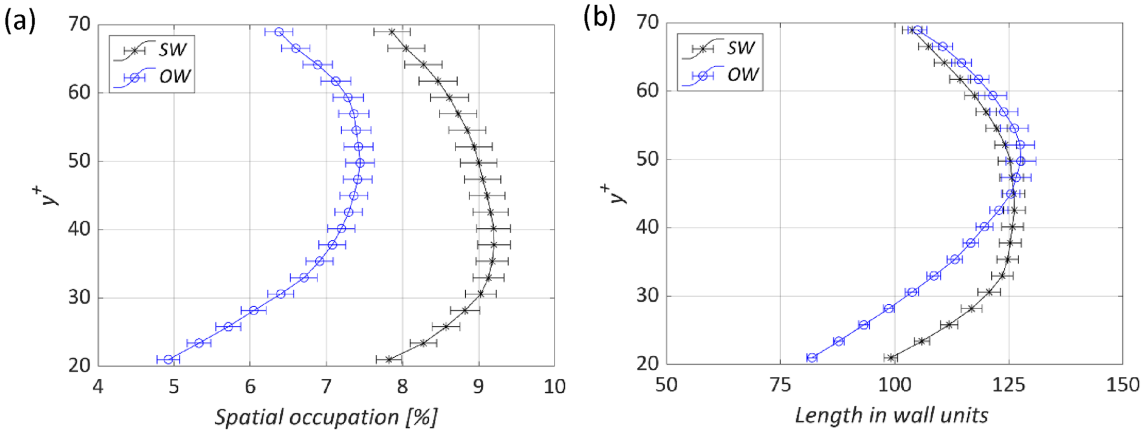

FIG. 15. Distribution of spatial occupation (a) and streamwise length (b) of the detected ejections in the measurement domain from the implementation of feature detection algorithm in each x–z plane corresponding to the wall-normal location.

ejection events. As a result, a primary hairpin vortex is created, which is followed by the formation of a hairpin packet through the auto-generation process.

The dynamical behavior recently hypothesized by the authors (Kempaiah *et al.*, 2020) hinges on the combined condition of pitched structures subject to a sidewise wall motion. This condition ultimately results in a sidewise tilt (γ) of the elongated structure and its rapid distortion as a result of the varying lateral friction induced by the moving wall. It is argued that not all phases of the oscillatory motion are effective in producing such distortion, the stages of maximum lateral velocity being most responsible for this mechanism. Instead, during the phase of motion inversion, when the wall can be considered stationary for a given time interval (approximately one/quarter of the total oscillation period), structure distortion remains minimal. The duration of such phase at $T^+ = 100$ is approximately 25 viscous time units and is comparable to the time reported for hairpin auto-generation ($t^+_{auto} = 30$). Therefore, the motion inversion phase is characterized by an increase in the number of hairpins. In contrast, the rapid motion of the wall during the phase of maximum lateral velocity inhibits the auto-generation process, due to the displacements of the streaks from the streamwise vortices, under the effect of the Stokes layer (Fig. 16).

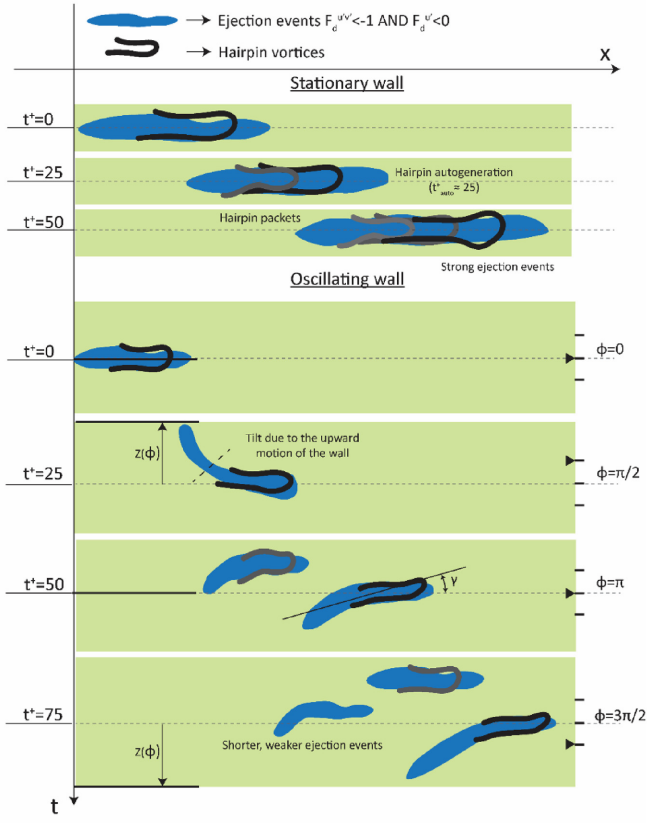

FIG. 16. Illustration of the distortion mechanism responsible for inhibiting hairpin auto-generation based on wall oscillation. The structure side-tilt results in shorter and less coherent ejections. The process is symmetrical around $\phi = \pi$.

From the obtained results, it is clear that the spanwise tilt of the identified structures is linked to the motion of the wall. This tilt imparted in the structures leads to a reduction in the length and spatial occupation of the ejection events [refer to Fig. 5 (multimedia view) for quantitative visualization of the detected structures for SW and OW]. The reduction in the intensity, length, and spatial occupation of the mixing events leads to a benefit in skin friction and a reduction in turbulent kinetic energy production. The above discussion is summarized and exemplified in the illustration, where the process of hairpin auto-generation in a turbulent boundary layer with a stationary wall is compared to that of an oscillating wall. For the latter, the salient features characterizing the different stages of the oscillation process are schematically illustrated.

IV. CONCLUSIONS

The low-speed streaks and ejection events in the near-wall region of a turbulent boundary layer at $Re_\theta = 1000$ subjected to spanwise wall oscillation have been investigated. Experimental data collected with tomographic-PIV are examined to infer the statistical properties of turbulence. Spatial auto correlation is compared with a feature-based technique to highlight the difference with respect to the coherent structures. The former returns limited information on the structure's properties and arrangement, which is due to wide spatiotemporal variations in their occurrence. Feature detection isolates the individual features of interest and is based on the instantaneous distribution of the Reynolds stress, in particular streamwise and wall-normal fluctuations. The spatial occupation and length of ejections are significantly reduced in the wall oscillation regime, 40% and 20%, respectively. Overall, the feature-based analysis appears to be more robust in these conditions and less affected by data dispersion during averaging.

The dependence of the turbulent motions on the phase of the wall motion has been further investigated. A clear phase dependence is observed between the sidewise tilt and the wall motion for the identified ejection events. Furthermore, a significantly higher probability for events with larger tilt is observed as a result of wall oscillation. The maximum observed tilt angle of approximately 20° is consistent with proposed estimates based on geometric or kinematic criteria. The streamwise length and spatial occurrence of streaks and ejections, instead, do not exhibit a specific correlation with the phase of the oscillation. The overall behavior and properties of streaks and ejections observed here are consistent with the conceptual model, whereby wall oscillations successfully weaken the early formation of hairpins in the near-wall cycle of the turbulent boundary layer by inhibiting hairpin auto-generation and, in turn, reducing the occurrence of energetic lift-up events.

ACKNOWLEDGMENTS

The authors would like to acknowledge the contribution of L. Bermel during experiments and the initial stages of data processing. In addition, the authors acknowledge the feedback and suggestion of the reviewers.

AUTHOR DECLARATIONS

Conflict of Interest

The authors have no conflicts to disclose.

Author Contributions

Kushal U. Kempaiah: Conceptualization (equal); Data curation (lead); Formal analysis (lead); Investigation (equal); Methodology (equal); Validation (equal); Visualization (lead); Writing – original draft (lead); Writing – review & editing (equal). **Fulvio Scarano:** Conceptualization (equal); Data curation (equal); Formal analysis (equal); Funding acquisition (lead); Investigation (equal); Methodology (equal); Project administration (equal); Resources (lead); Software (equal); Supervision (equal); Validation (equal); Visualization (supporting); Writing – original draft (equal); Writing – review & editing (equal).

DATA AVAILABILITY

The data that support the findings of this study are available within the supplementary material.

APPENDIX: SENSITIVITY OF THE RESULTS ON THE CHOICE OF THRESHOLD

The proposed analysis is based on a detection algorithm, where a threshold level is chosen that identifies relevant events. In this appendix, the detection of ejection events is considered ($F_d^{u'v'} < -F_t \,\&\, F_d^{u'} < 0$), and the results are examined while varying the threshold level (F_t) from –0.5 to −2.0. The analysis compares the conditions of stationary (SW) and oscillating wall (OW). The present analysis is performed to indicate the dependence of results upon the value of the chosen threshold and the proposed approach's validity range. The effects on spatial occupation, length scale, and the sidewise tilt (γ) of the identified ejection events are scrutinized.

The spatial occupation of ejections decreases as F_t is increased (in absolute value) from −0.5 to −2.0. This trend is repeated for both SW and OW (Fig. 17). Such reduction is expected, as only more intense regions of Reynolds stress are selected by a more stringent threshold ($F_t < -2.0$). In the context of comparing SW and OW conditions, the ratio of the spatial occupation appears to remain relatively unchanged by the choice of the threshold, with average values of 1.25 ($F_t < -0.5$), 1.28 ($F_t < -1.0$), and 1.45 ($F_t < -2.0$). The relative increase for the more stringent value of the threshold indicates that events with high amplitude tend to become rare in the OW regime.

The length scale of these events is reported in Table IV. The results exhibit similar behavior to that of spatial occupation. The average length of the identified event reduces with a more stringent choice for the threshold. Intense ejection events are rather focused and occur in isolated regions in the flow field. This can also be observed in the contour plots of the detection function in Fig. 4(d) (refer to article), where areas with $F_t < -2.0$ depict a specific region that satisfies the detection criterion. Also, in this case, the amount of length reduction of the events for the OW with respect to the SW expressed by their ratio is maintained constant, with some exceptions for $F_t < -2.0$.

An important structural parameter is the sidewise tilt of the structures. It is expected that if the similarity is maintained by varying the threshold value, the tilt angle will remain unchanged.

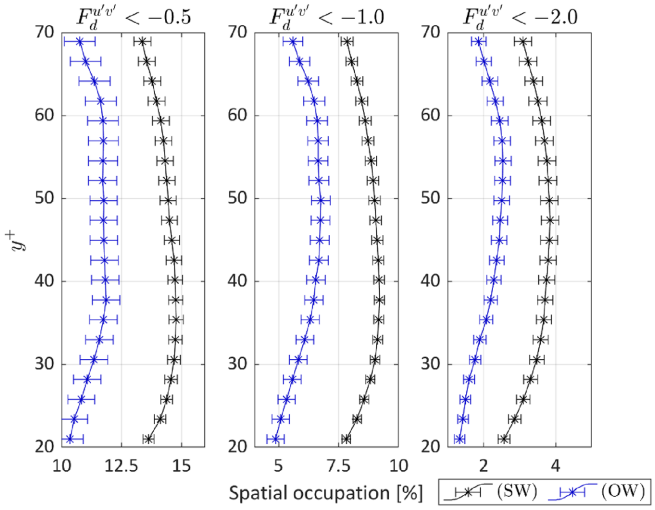

FIG. 17. Spatial occupation for variation of the threshold value of −0.5, −1.0, and −2.0 for stationary wall (SW) and oscillating wall (OW, corresponds to $\phi = \pi/4$).

TABLE IV. Sensitivity analysis of the threshold constant.

Ejection events ($F_d^{u'v'} < -F_t$ and $F_d^{u'} < 0$)		$F_t = -0.5$	$F_t = -1$	$F_t = -2$
Length (wall units$^+$)	SW	229 ± 8	194 ± 6	143 ± 4
	OW ($\phi = \pi/4$)	199 ± 12	168 ± 10	138 ± 7
Ratio		1.15	1.15	1.04

In Fig. 18, the occurrence of side tilt is displayed for the three chosen values of F_t. For the SW regime, the diagram remains symmetrical, with a slight reduction of the central maximum. The latter is ascribed to the more frequent detection of smaller and isotropic structures, which tends to homogenize the distribution of their angle. Earlier in this work, a reference value of the tilt angle $\gamma_0 = 25°$ was defined based on flow and wall kinematics. When the threshold value is varied, the occurrence of side tilt shows a secondary peak around such value for $F_t < -1$ and $F_t < -2$. For $F_t < -0.5$, the difference between the SW and OW is more scattered, and no distinct peak can be inferred. From the above, it can be concluded that wall oscillations affect intense events in a more pronounced way.

From the above, it may be concluded that the choice of the threshold has an effect on the absolute values found for spatial occupation and length. However, for the purpose of comparing the regimes of SW and OW, a choice of the threshold within half to double the unit value will still return consistent observations. Furthermore, it may be conjectured that, given the non-dimensional definition of the properties chosen for identification, it is expected that the choice of a threshold value may not need to be revised when considering different turbulent regimes or wall actuation conditions. Nonetheless, the latter remains to be demonstrated by further experiments and numerical simulation studies.

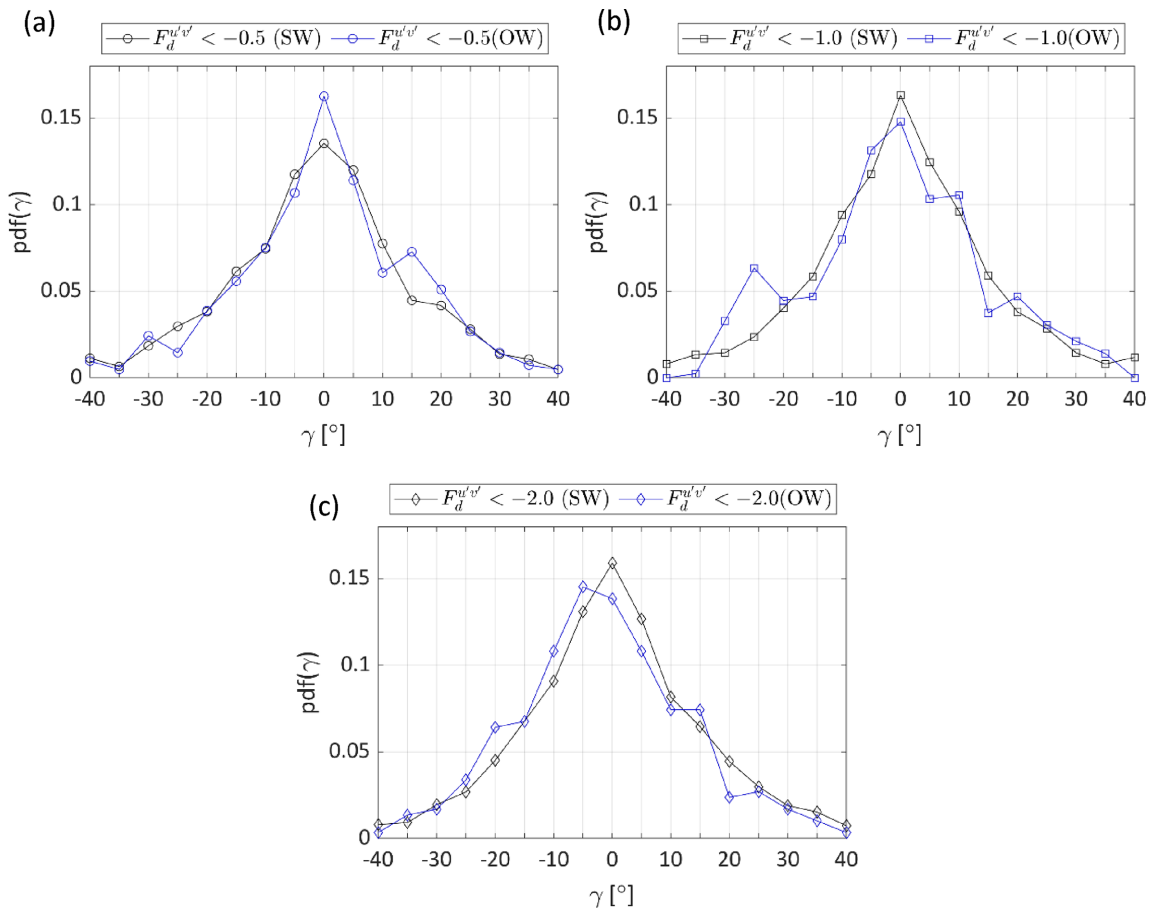

FIG. 18. Probability distribution of sidewise tilt (γ) from detected ejections for variation of the threshold value of -0.5 (a), -1.0 (b), and -2.0 (c) for stationary wall (SW) and oscillating wall (OW, corresponds to $\phi = 3\pi/4$).

REFERENCES

Adrian, R. J., Meinhart, C. D., and Tomkins, C. D., "Vortex organisation in the outer region of the turbulent boundary layer," J. Fluid Mech. **422**, 1–54 (2000).

Adrian, R. J., "Hairpin vortex organisation in wall turbulence," Phys. Fluids **19**(4), 041301 (2007).

Bae, H. J., and Lee, M., "Life cycle of streaks in the buffer layer of wall-bounded turbulence," Phys. Rev. Fluids **6**(6), 064603 (2021).

Baron, A., and Quadrio, M., "Turbulent drag reduction by spanwise wall oscillations," Appl. Sci. Res. **55**(4), 311–326 (1995).

Blackwelder, R. F., and Kaplan, R. E., "On the wall structure of the turbulent boundary layer," J. Fluid Mech. **76**(1), 89–112 (1976).

Cimarelli, A., Frohnapfel, B., Hasegawa, Y., De Angelis, E., and Quadrio, M., "Prediction of turbulence control for arbitrary periodic spanwise wall movement," Phys. Fluids **25**(7), 075102 (2013).

Choi, K. S., "Near-wall structure of turbulent boundary layer with spanwise-wall oscillation," Phys. Fluids **14**(7), 2530–2542 (2002).

Elsinga, G. E., Scarano, F., Wieneke, B., and van Oudheusden, B. W., "Tomographic particle image velocimetry," Exp. Fluids **41**(6), 933–947 (2006).

Ganapathisubramani, B., Longmire, E. K., and Marusic, I., "Characteristics of vortex packets in turbulent boundary layers," J. Fluid Mech. **478**, 35–46 (2003).

Haralick, R. M., and Shapiro, L. G., *Computer and Robot Vision* (Addison-Wesley, 1992), Vol. I, pp. 28–48.

Head, M. R., and Bandyopadhyay, P., "New aspects of turbulent boundary-layer structure," J. Fluid Mech. **107**, 297–338 (1981).

Jodai, Y., and Elsinga, G. E., "Experimental observation of hairpin autogeneration events in a turbulent boundary layer," J. Fluid Mech. **795**, 611 (2016).

Jung, W. J., Mangiavacchi, N., and Akhavan, R., "Suppression of turbulence in wall-bounded flows by high-frequency spanwise oscillations," Phys. Fluids A **4**(8), 1605–1607 (1992).

Kempaiah, K. U., Scarano, F., Elsinga, G. E., van Oudheusden, B. W., and Bermel, L., "3-dimensional particle image velocimetry based evaluation of turbulent skin-friction reduction by spanwise wall oscillation," Phys. Fluids **32**(8), 085111 (2020).

Kline, S. J., Reynolds, W. C., Schraub, F. A., and Runstadler, P. W., "The structure of turbulent boundary layers," J. Fluid Mech. **30**(4), 741–773 (1967).

Laadhari, F., Skandaji, L., and Morel, R., "Turbulence reduction in a boundary layer by a local spanwise oscillating surface," Phys. Fluids **6**(10), 3218–3220 (1994).

Leschziner, M. A., "Friction-drag reduction by transverse wall motion—A review," J. Mech. **36**(5), 649–663 (2020).

Lu, S. S., and Willmarth, W. W., "Measurements of the structure of the Reynolds stress in a turbulent boundary layer," J. Fluid Mech. **60**(3), 481–511 (1973).

Martins, F. J., Foucaut, J. M., Stanislas, M., and Azevedo, L. F., "Characterisation of near-wall structures in the log-region of a turbulent boundary layer by means of conditional statistics of tomographic PIV data," Exp. Therm. Fluid Sci. **105**, 191–205 (2019).

Marusic, I., Chandran, D., Rouhi, A., Fu, M. K., Wine, D., Holloway, B., Chung, D., and Smits, A. J., "An energy-efficient pathway to turbulent drag reduction," Nat. Commun. **12**(1), 5805 (2021).

Moin, P., Leonard, A., and Kim, J., "Evolution of a curved vortex filament into a vortex ring," Phys. Fluids **29**(4), 955–963 (1986).
Quadrio, M., and Ricco, P., "Critical assessment of turbulent drag reduction through spanwise wall oscillations," J. Fluid Mech. **521**(12), 251–271 (2004).
Schlatter, P., and Örlü, R., "Assessment of direct numerical simulation data of turbulent boundary layers," J. Fluid Mech. **659**, 116 (2010).
Schröder, A., Geisler, R., Staack, K. É., Elsinga, G. E., Scarano, F., Wieneke, B., Henning, A., Poelma, C., and Westerweel, J., "Eulerian and Lagrangian views of a turbulent boundary layer flow using time-resolved tomographic PIV," Exp. Fluids **50**(4), 1071–1091 (2011).
Sillero, J. A., Jiménez, J., and Moser, R. D., "Two-point statistics for turbulent boundary layers and channels at Reynolds numbers up to $\delta+ \approx 2000$," Phys. Fluids **26**(10), 105109 (2014).
Tong, F., Dong, S., Lai, J., Yuan, X., and Li, X., "Wall shear stress and wall heat flux in a supersonic turbulent boundary layer," Phys. Fluids **34**(1), 015127 (2022).
Touber, E., and Leschziner, M. A., "Near-wall streak modification by spanwise oscillatory wall motion and drag-reduction mechanisms," J. Fluid Mech. **693**(2), 150–200 (2012).
Wallace, J. M., "The vortical structure of bounded turbulent shear flow," in *Flow of Real Fluids* (Springer, Berlin, Heidelberg, 1985), pp. 253–268.
Wallace, J. M., Eckelmann, H., and Brodkey, R. S., "The wall region in turbulent shear flow," J. Fluid Mech. **54**(1), 39–48 (1972).
Yakeno, A., Hasegawa, Y., and Kasagi, N., "Modification of quasi-streamwise vortical structure in a drag-reduced turbulent channel flow with spanwise wall oscillation," Phys. Fluids **26**(8), 085109 (2014).